Received: 23 June 2021 | Revised: 13 August 2021 | Accepted: 21 September 2021

DOI: 10.1111/ffe.13589

ORIGINAL ARTICLE

FFEMS Fatigue & Fracture of Engineering Materials & Structures WILEY

Small-sized specimen design with the provision for high-frequency bending-fatigue testing

Hamed Ghadimi | **Arash P. Jirandehi** | **Saber Nemati** | **Shengmin Guo**

Department of Mechanical and Industrial Engineering, Louisiana State University, Baton Rouge, Louisiana, USA

Correspondence
Shengmin Guo, Department of Mechanical and Industrial Engineering, Louisiana State University, Baton Rouge, LA 70803, USA.
Email: sguo2@lsu.edu

Funding information
National Science Foundation, Grant/Award Number: OIA-1946231; U.S. Department of Energy (Office of Science, Office of Basic Energy Sciences and Energy Efficiency and Renewable Energy, Solar Energy Technology Program), Grant/Award Number: DE-SC0019378; Louisiana Board of Regents for the Louisiana Materials Design Alliance (LAMDA)

Abstract

The testing and study of emerging materials—such as additively manufactured materials—demands for specimen designs that are cost effective and time saving. The design of a small-sized bending-fatigue test specimen for an ultrasonic fatigue testing system is reported in this paper. The design is optimized based on the finite element analysis and analytical-solution results to achieve the proper vibration shape and stress distribution. The proposed design is evaluated in the high- and very-high-cycle fatigue regimes under 20-kHz frequency. Both simulation and testing results confirm that the desirable vibration mode occurs and the specimen fails at the designated test (gauge) section, where the maximum stress exists. The stress–life (*S*–*N*) curve is obtained for Inconel alloy 718 and indicates an expected trend.

KEYWORDS

additive manufacturing, bending-fatigue, high-cycle fatigue, high-frequency fatigue testing, small-sized specimen

1 | INTRODUCTION

Fatigue testing at high- and very-high-cycle life regimes is time consuming and costly. However, it is crucial for many engineering applications, in particular for automotive, aerospace, and railway applications.[1–4] To perform high-cycle fatigue (HCF) experiments, ultrasonic fatigue testers overcome the time- and cost-related limitations associated with traditional fatigue testing machines, such as mechanical driven machines (eccentric crank, power screws, and rotating), electromechanical or magnetically driven machines, or hydraulic/electrohydraulic driven machines.[5] Using an ultrasonic fatigue tester operating at 20-kHz frequency, 10 billion fatigue life cycles in the very-high-cycle regime can be achieved in less than 6 days. Ultrasonic fatigue testers are used for HCF/very-high-cycle fatigue regimes (VHCF), as a rapid testing method. Nonetheless, high-frequency testing apparatus have stringent requirements for their specimen design, including shape, size, surface finish, and geometrical tolerance.

Ultrasonic fatigue testing systems were employed for studying the fatigue behavior of materials in different fatigue testing types since they first constructed in 1950.[6,7] Although torsional[8] and three-point bending multiaxial[9] ultrasonic fatigue tests were later developed, high-frequency uniaxial tension–compression fatigue testing studies are more studied in the literature.[10–12] Ultrasonic fatigue tests are generally carried out on specimens of sufficient length to resonate in ultrasonic frequency. Methods for the ultrasonic fatigue testing of various designs such as cruciform specimen[13]—biaxial—and even thin sheets have also been developed.[7] In addition to fatigue tests in the ambient temperature, ultrasonic fatigue equipment also developed and used for tests in high[14] and cryogenic[15] temperatures. In addition, fretting fatigue property of different materials is also studied using ultrasonic testing systems.[16]

A wealth of studies is dedicated to characterizing the behavior of materials made with different methods by exposing them to static and cyclic loads under different environmental conditions.[4,17–24] In recent years, the mechanical performance of additively manufactured (AM) materials has caught the attention of research communities due to their extensive applications.[25–29] Despite the conducted research up to this point, many aspects of the AM materials are still less explored. For example, given the high level of flaws observed in AM parts' microstructures, it is important to distinctly study their performance under different load types. Developing new AM alloys, investigating proper AM design, and studying the effects of AM build parameters on the mechanical performance require fabrication of various types and number of AM test specimens. In particular, to assess the effect of such parameters on material's mechanical performance under cyclic loading (aka fatigue),[30–34] a large number of test specimens are required.

Utilizing subsized specimens for the fatigue-related studies has been repeatedly reported in the literature.[35–37] Small-sized specimens are commonly introduced and used when limited amount of testing material is available, for the determination of fatigue properties for nanostructured materials, assessment of dilatometric samples used for thermal and thermomechanical treatment development, local properties of weld joints, and so on.[38] In addition, a wide variety of metallic mechanical parts and components are in the form of sheets—such as metal bellows and belts—where the thin sheet fatigue properties need to be studied.[39] Utilizing subsized samples also enables the study of residual service life assessment of in-service components and local properties determination for anisotropic properties assessment.[37] The primary motivation behind this study is its potential advantage for AM material testing. The scientific barrier to accomplish the rapid qualification of metallic AM parts is the lack of high-fidelity processing strategy–structure–performance (PSP) relationships. Laser-based AM is a process far from equilibrium, resulting in a wide spectrum of kinetically stabilized microstructures and pores/cracks that span multiple length scales. To address these challenges, a thorough understanding of complex microstructure (including pores and cracks) formation/evolution during the fabrication process and under mechanical loading is needed to increase the confidence in tailoring the AM processing strategies to achieve the desired performance of parts.

The authors plan to link complex AM processing strategies to mechanical and functional performance by establishing correlations among processing strategy, microstructure (including pores/cracks), and mechanical performance on mesoscale building strategy sets. The mesoscale building strategy sets are defined as a collection of localized laser scan strategies (variations among adjacent tracks and among adjacent layers), machine processing parameters (such as the ventilation flow speed and direction), thermal history, and local powder/substrate characteristics that will result in definitive microstructures (including pores/cracks) and mechanical performance in a quantifiable small volume (the discrete building volume). Specimens with very small gauge volume for fatigue assessment (this study) could be used to establish the detailed PSP relationships for discrete building volumes of AM parts. This study is the first step towards this big goal. The small sheet specimens are not necessarily be AM made directly. The authors have successfully machined small sheet specimens out of AM blocks using wire electrical discharge machining (EDM). Of course, the location of the specimens in the original AM block should be known, together with the related local AM processing parameters. This would enable the establishment of detailed PSP relationships for AM building strategy sets in the future. For small samples, the 3D microstructure information can be obtained from nondestructive evaluation (NDE) methods such as X-ray computed tomography (CT) scans.[40] Modern X-ray CT can detect micron-sized defects in metallic samples with a cross-section of a few millimeter range.[41] Knowing such micron-sized defects in AM parts can significantly improve the understanding to the fatigue life performance.

During a fatigue test, a crack first incubates in the specimen—the crack initiation phase—and then propagates to a critical length at failure—the crack propagation phases. Structural defects play a major role in the crack initiation phase.[42–45] From this standpoint, clearly quantified defect information regarding the fatigue samples is extremely beneficial for fatigue studies. As mentioned previously, in order to achieve the defect detection resolution in the order of a micron by X-ray CT, the metallic sample size is limited to a few millimeters. Considering that fatigue tests have to be repeated multiple times to achieve statistically meaningful results, preparing multiple conventional samples for testing is a costly and time-consuming process.[46] In contrast, small-sized test specimens are beneficial from the affordability point of view as they make the study of a wider processing window more affordable and thus facilitate the production of more quantifiable specimens under a variety of processing conditions.

The above-mentioned points motivated this study and led to the design of a small-sized test specimen for high-frequency bending-fatigue testing. Although large number of studies on uniaxial tension–compression fatigue of

AM specimens are available in literature,[15,47–49] the bending-fatigue testing of AM materials with small-sized specimens particularly with provisions for high-frequency testing is studied less. Therefore, in this study, the design for a small-sized bending-fatigue test specimen is discussed as well as the test setup using an ultrasonic fatigue testing system. Using finite element and theoretical solutions, the vibration response of the designed specimen (including natural frequencies, mode shapes, and stress/strain distribution) and its fatigue performance are investigated. In order to evaluate the proposed specimen design, Inconel alloy 718 test specimens are fabricated conventionally, and the stress–life curve is obtained using the ultrasonic bending-fatigue test setup.

2 | SMALL-SIZED SPECIMEN DESIGN FOR HIGH-FREQUENCY BENDING-FATIGUE TESTING

2.1 | The existing fatigue testing system

A SHIMADZU USF-2000A ultrasonic fatigue testing system is used in this study. The USF-2000A system is originally designed to generate tension–compression stress in a tapered/straight rod-shaped testing specimen by resonating the sample with 20-kHz longitudinal wave oscillation. The ultrasonic resonance system includes a power supply, an ultrasonic oscillator, a booster, and a horn (see Figure 1). An electric signal with defined amplitude and frequency is generated in the power supply. Then, a piezoelectric actuator/transducer element is employed to transform the electrical signal to acoustic wave (displacement). A booster and an acoustic horn are installed in between the specimen and the converter to adjust/amplify the input wave to the desired load/displacement at the specimen gauge section. Because the booster and the horn operate and resonate at 20 kHz, the test specimen must be designed to experience the desirable vibration mode at the frequency of 20 kHz for performing constant stress/strain cyclic tests.

The operation principle of the fatigue testing system is shown in Figure 1. During oscillations, the top and bottom displacements of the specimen are equal, and the specimen's center remains at the same height. Based on the material properties and the amplitude of the vibration (A_0), the maximum stress applied at the center of the specimen can be calculated. Figure 2 shows the shape of stainless steel tapered/straight rod-shaped test specimens for tension–compression fatigue testing. Although the specimen dimensions may change for different metals, the shape of the design stays the same.

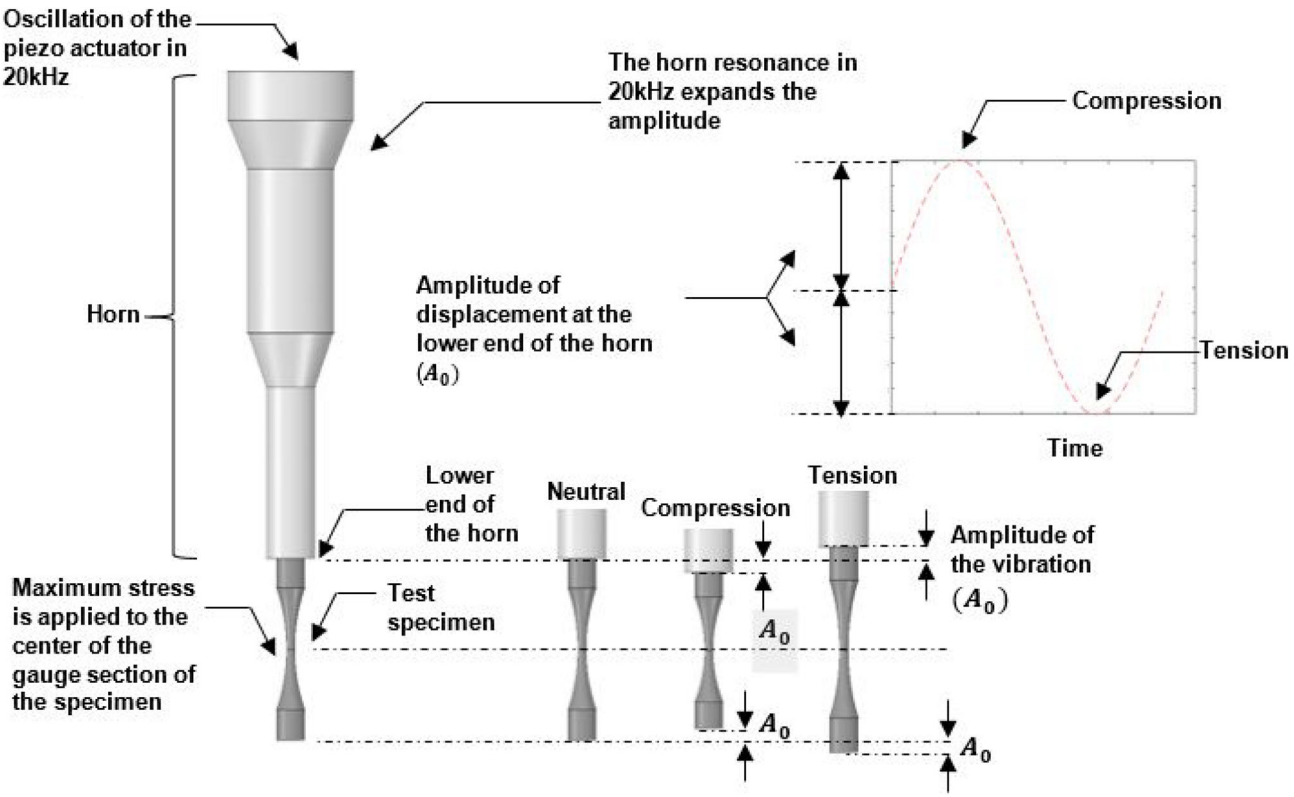

FIGURE 1 The operation principle of the high-frequency fatigue system in use [Colour figure can be viewed at wileyonlinelibrary.com]

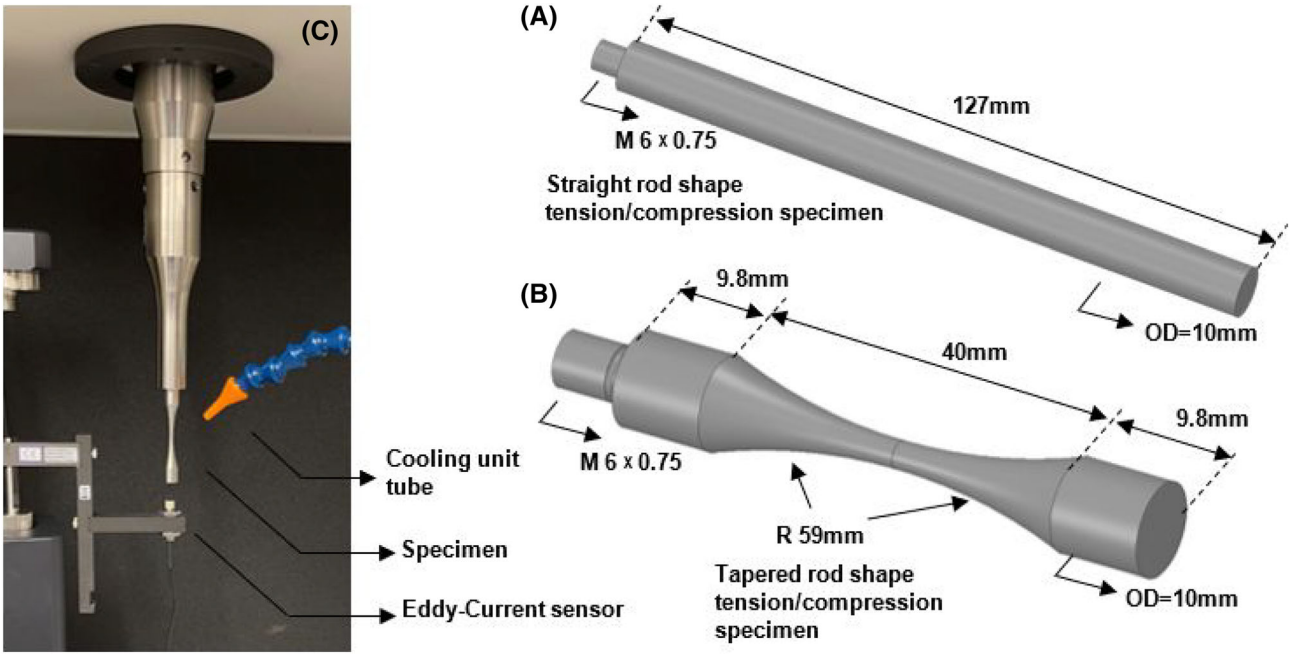

FIGURE 2 SHIMADZU USF-2000A tester is designed for high-frequency tension/compression fatigue testing; (A) straight rod-shaped specimen, (B) tapered rod-shaped specimen (sizes are for stainless steel material), and (C) testing arrangement [Colour figure can be viewed at wileyonlinelibrary.com]

To obtain the longitudinal movement of the specimen, a high-speed eddy-current sensor is employed, as seen in Figure 2. Because the ultrasonic fatigue tests are performed within the elastic limit of the specimen, the stress value of the specimen can be calculated based on the displacement amplitude. Additionally, because the temperature of the specimen increases during the fatigue test due to the high frequency of testing, a cooling system with a compressed air jet is used to keep the temperature of the specimen below 30°C (considering a room temperature of around 25°C). The general setup for the ultrasonic tension–compression fatigue tests includes the test specimen, an eddy-current sensor for displacement measurement, and a cooling system for specimen temperature control make up (Figure 2).

2.2 | Bending-fatigue testing arrangement for small-sized specimen

As explained in Section 2.1, the USF-2000A ultrasonic fatigue testing system is designed to apply tension–compression loads on the straight/tapered rod-shaped test specimens. In general, the specimens for ultrasonic fatigue testers are smaller in size relative to the conventional fatigue specimens. Nonetheless, when using additive manufacturing to fabricate the samples, further reducing the size can be more beneficial and facilitating from a manufacturing standpoint. In order to test small AM samples, a thin-plate small-sized specimen is proposed to fit into the system for bending-fatigue tests (Figure 3). The small-sized bending specimen is nestled between a straight rod-shaped tension–compression specimen and the horn. To keep enough distance between the upper face of the specimen and the lower face of the horn's tip, a spacer washer is also placed on top of the bending specimen. The rod specimen is fixed into the horn using the specimen fixer shown in Figure 3. An eddy-current sensor (see Figures 2 and 3) is also used in the bending-fatigue setup to measure the applied amplitude/displacement at the free end of the straight rod (as introduced in Section 2.1). It is worth noting that the straight rod in Figure 3 serves both as a specimen holder when conducting the bending-fatigue tests in this study and also reading the applied displacement by the fatigue tester. It goes without saying that this measured amplitude is equal to the displacement amplitude at the fixed end of the bending-fatigue specimen (A_0).

2.3 | Bending-fatigue specimen design approach and preparation

Important considerations around the proper design of a small-sized bending-fatigue specimen include the natural

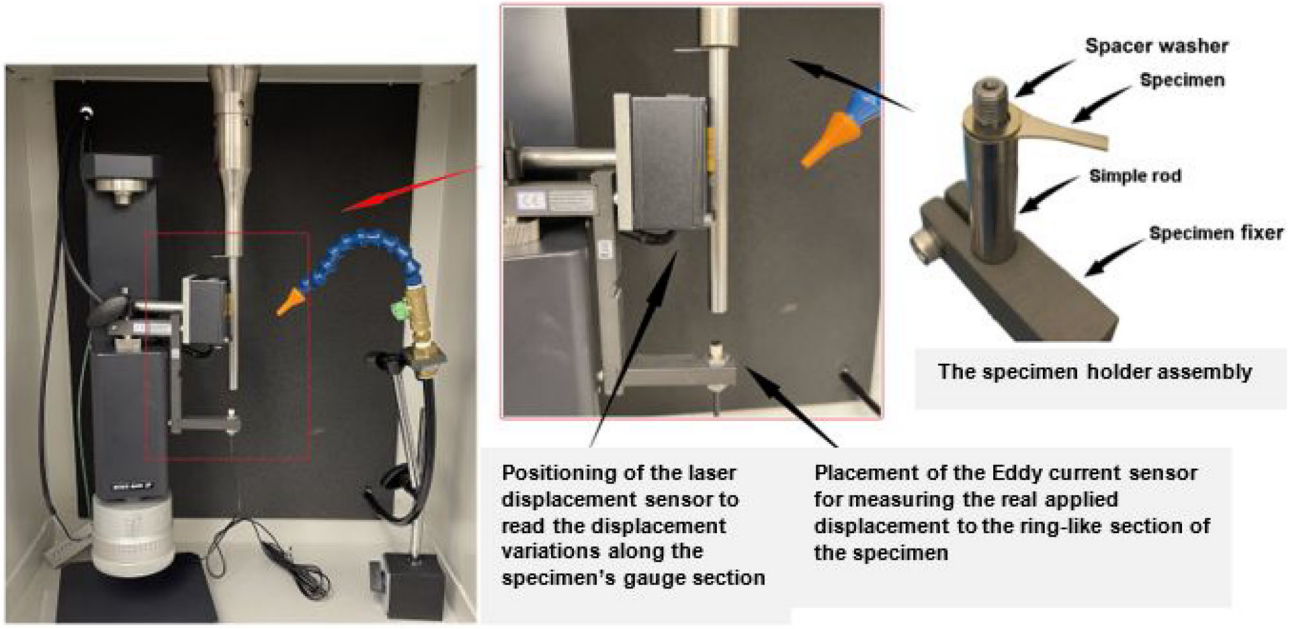

FIGURE 3 Bending-fatigue testing setup using SHIMADZU USF-2000 ultrasonic tester [Colour figure can be viewed at wileyonlinelibrary.com]

frequency, the vibration shape of the specimen, and the induced stress distribution. For the testing system to resonate at 20-kHz frequency, the natural frequency of the entire system (including the horn, the straight rod, and the new bending-fatigue specimen) should be kept within an acceptable frequency range. Also, the induced stress distribution within the small-sized specimen must be suitable for bending-fatigue testing. In addition, the designed specimen should have a geometry allowing it to fit into the device easily. Accordingly, the specimen's vibration shape and bending mode, as well as the stress distribution along its length, are investigated. Section 2.3.1 describes the design approach leading to an optimized design, after a brief discussion regarding the baseline design.

2.3.1 | Baseline shape of small-sized bending-fatigue specimen

The baseline design mentioned in this study has a rectangular shape in the gauge section (Figure 4) and is used in a technical report from SHIMADZU,[50] where SHIMADZU implemented a high-speed video camera to observe the movement of a metal plate vibrating at 20 kHz. This SHIMADZU report confirms that the addition of the small-sized bending-fatigue specimen—with a small mass—does not affect the overall system resonance frequency and the ultrasonic fatigue testing system could still operate properly. In the current study, the same baseline design of bending-fatigue specimen was cyclically loaded via the SHIMADZU ultrasonic fatigue tester in the HCF and VHCF regimes.

To fabricate the bending-fatigue test specimens, wire EDM is used. First, the baseline design specimens are fabricated and prepared; then, the high-frequency bending-fatigue test is performed. Throughout the experiments, it is unanimously seen that the specimens with the baseline design break from the root region (Figure 4). The stress concentration at the root of these test specimens causes cracks to emerge there and failure occurs from those points. Because the distribution and nature of the stresses in this region are complex, this area cannot be used as a the gauge section to study fatigue behavior. Therefore, it can be concluded that the baseline specimen design is not the best choice for bending-fatigue tests. The optimized design—the main outcome of this study—is discussed in the next section and is shown in Figure 5.

2.3.2 | Optimized shape of small-sized bending-fatigue specimen

The optimized shape for small-sized bending-fatigue test specimen (Figure 5) is designed to avoid stress concentration and the subsequent premature failure of the specimens. For this purpose, the gauge section is

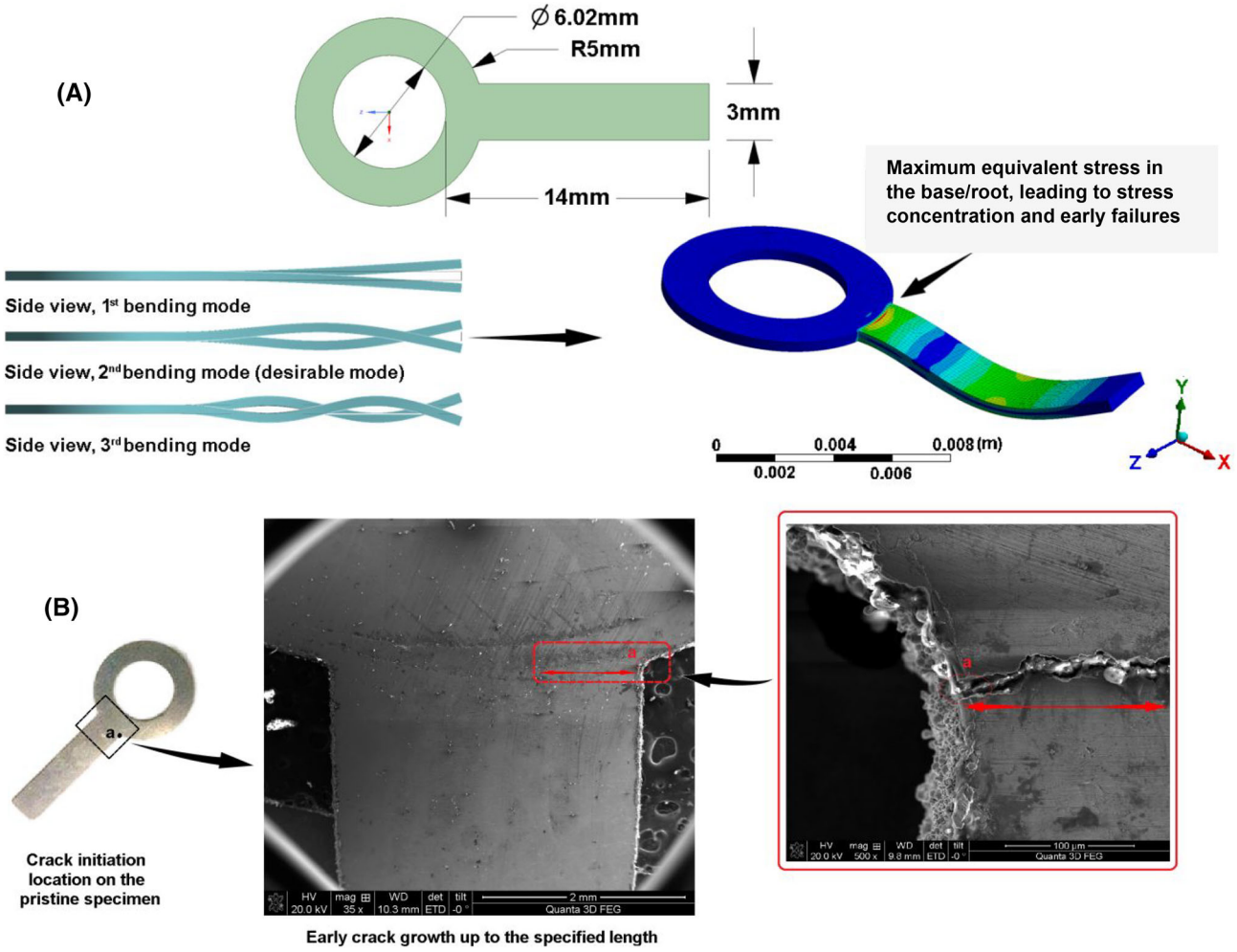

FIGURE 4 (A) Baseline design of bending-fatigue testing specimen and (B) crack initiation location on the baseline specimen, starting from the stress-concentrated corners leading to early crack growth [Colour figure can be viewed at wileyonlinelibrary.com]

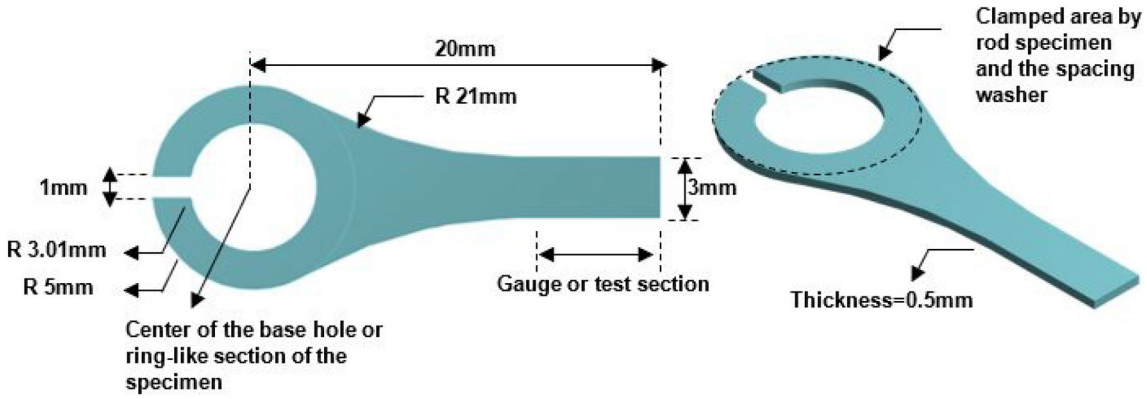

FIGURE 5 Optimized design of high-frequency bending-fatigue testing specimen (sizes are for Inconel alloy 718 material) [Colour figure can be viewed at wileyonlinelibrary.com]

designed to stay away from the root. The natural frequency of the geometry is investigated, as well as the shape of the bending mode and the stress/strain distribution. The analyses in Sections 3 and 4 show that the design (shown in Figure 5) can be viably used for high-frequency bending-fatigue testing.

2.4 | Experimental methodology

2.4.1 | Material for validation testing

Inconel alloy 718 sheet metal is used in this study to validate the design. Inconel alloy 718 benefits from good mechanical strength and the ability to undertake moderate-to-high levels of deformation, that is, 50% elongation at break. Table 1 shows the chemical compositions of Inconel alloy 718, and Table 2 indicates its mechanical properties. The finite element analysis (FEA) simulations and the theoretical analysis (Sections 3–5) are based on these Inconel alloy 718 material properties.

2.4.2 | Specimen polishing process

In order to obtain fatigue test specimens with smooth and mirror-finished surface, they were polished using a single-wheel metallographic manual polisher (with various grades of sandpaper) and a vibratory polisher. Additionally, before and after polishing, the thicknesses of the specimens' gauge section were measured with a micrometer in various spots to ensure consistent thickness across the specimen (see Figure 5). The specimens are glued to the polishing face of the specimen holder after they were cleaned (see Figure 6). Finally, the polished specimens were inspected using scanning electron microscopy (SEM) for signs of surface roughness in order to assess the polishing quality.

The specimens are polished in three steps. First, a single-wheel metallographic manual polisher is used to manually polish the specimens. In this step, adhesive-back metallographic silicon carbide polishing pads with grits of 800, 1000, and 1200 were used. A single-wheel metallographic manual polisher with 6, 3, and 1 micron metallographic polycrystalline diamond abrasives and magnetic polishing pads was used for the second step of polishing. When using manual polishers in the first and the second steps, the specimens were polished along their longitudinal axis to achieve better quality. The final step was accomplished via a vibratory polisher and proper metallographic final polishing abrasive. The specimens were polished for 24 h at the proper frequency in the vibratory polisher. After vibratory polishing, the specimen was separated from the holder, and the polishing process was repeated on the opposite side of the test specimen. At this point, the polished specimens' thickness was measured, and the polishing quality of specimens was examined using SEM. Following the explained polishing procedures, a 5% reduction in thickness was observed, which is included in the calculations.

2.4.3 | Experimental vibration shape measurement

To measure the displacements of the gauge section of the small-sized test specimen under vibration, a KEYENCE LK-G5000 high-speed laser displacement sensor with a maximum sampling frequency of 500 kHz is employed. For each specified location along the specimen's gauge section (Figure 7), displacement readings were recorded at 2-μs intervals. The displacements along the specimen are measured to confirm the vibration mode/shape. The markings on the test specimen and the arrangements used to study the shape of the specimen while vibrating at 20 kHz are shown in Figure 7. The acquired data for the amplitudes of oscillation are extracted and discussed in Section 4.

3 | ANALYTICAL AND NUMERICAL STUDY OF THE VIBRATION SHAPE

In order to optimize the specimen shape, analytical solution and FEA are performed. FEA is also used to assess the stress level across the gauge section of the specimens.

3.1 | Analytical

The vibration response of the bending-fatigue test specimen is modeled and solved as a cantilevered beam

TABLE 1 Composition (wt%) for Inconel 718

C	Mn	Fe	S	Si	Cu	Ni	Cr	Al	Ti	Co	Mo	Ta	B	Nb	P
0.03	0.07	18.36	0.001	0.06	0.04	53.45	18.30	0.52	0.94	0.10	2.98	0.01	0.003	5.07	0.011

TABLE 2 Mechanical properties of the tested Inconel 718 in this study

Density (kg/m^3)	Tensile yield strength (MPa)	Tensile ultimate strength (MPa)	Modulus of elasticity (MPa)
8195	490	910	2.08×10^5

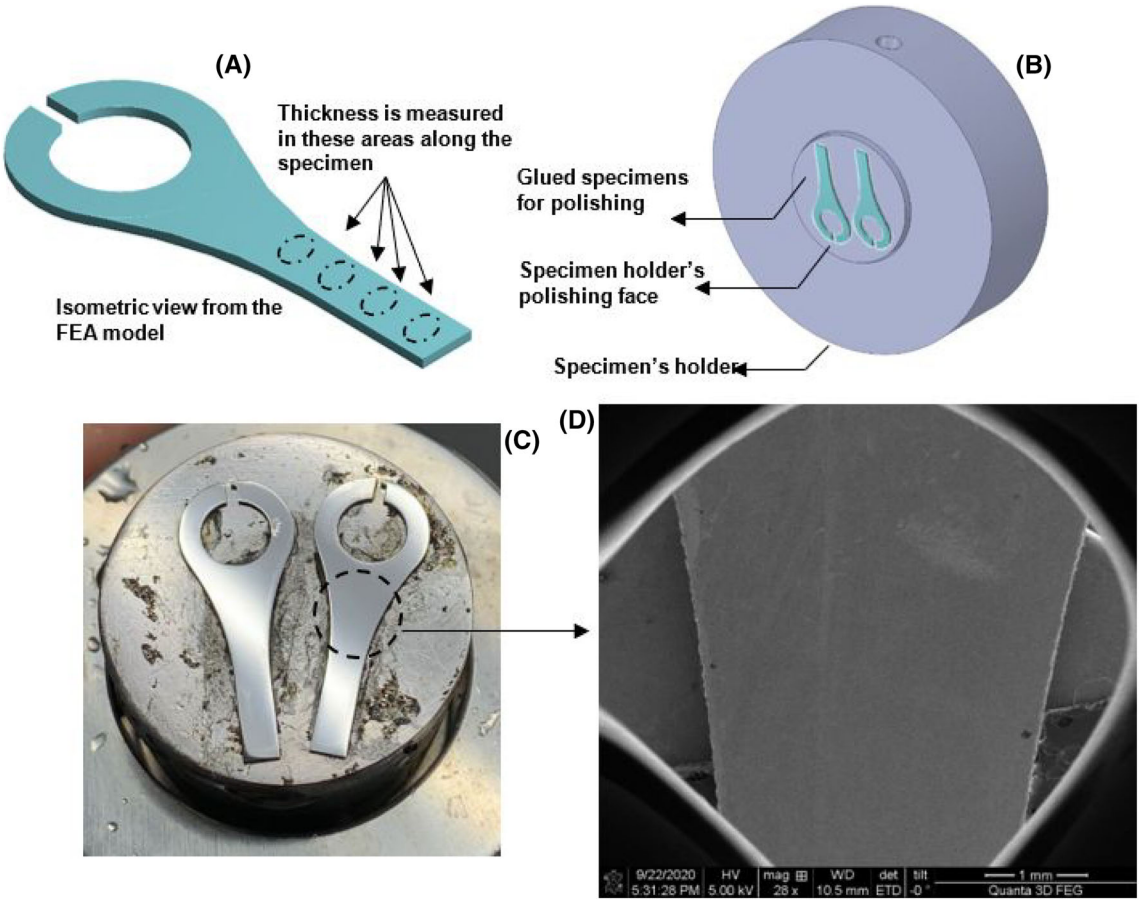

FIGURE 6 Polishing of the specimens via the metallographic polisher; (A) specimen holder configuration for polishing and (B) the scanning electron microscopy (SEM) image from the polished specimen showing a smooth surface [Colour figure can be viewed at wileyonlinelibrary.com]

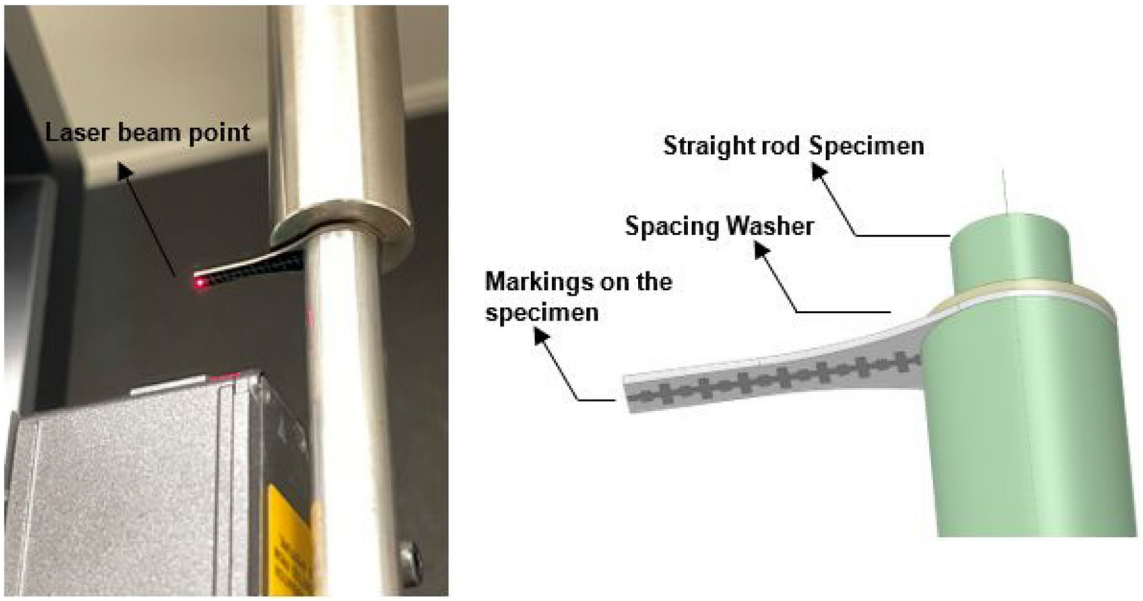

FIGURE 7 The marked specimen for vibrational mode study [Colour figure can be viewed at wileyonlinelibrary.com]

with a frequency of 20 kHz and an amplitude of A_0 at the base (fixed end). Because the maximum amplitude of the specimen's tip (Max ≈ 70 μm) is less than the thickness of the specimen (≈500 μm) and the specimen's length exceeds 10 times its thickness, the governing equation are eligible for small deflection assumption. Euler–Bernoulli beam theory is implemented in the MATLAB programming environment to study the deflections and forced vibration characteristics of the specified beam.[51,52] Figure 8A displays a cantilever beam with the supports and applied loads, as well as the internal forces acting on a portion of the beam. $f(x,t)$ is the applied distributed force on the beam per unit length which is a function of location and time. M and V represent internal

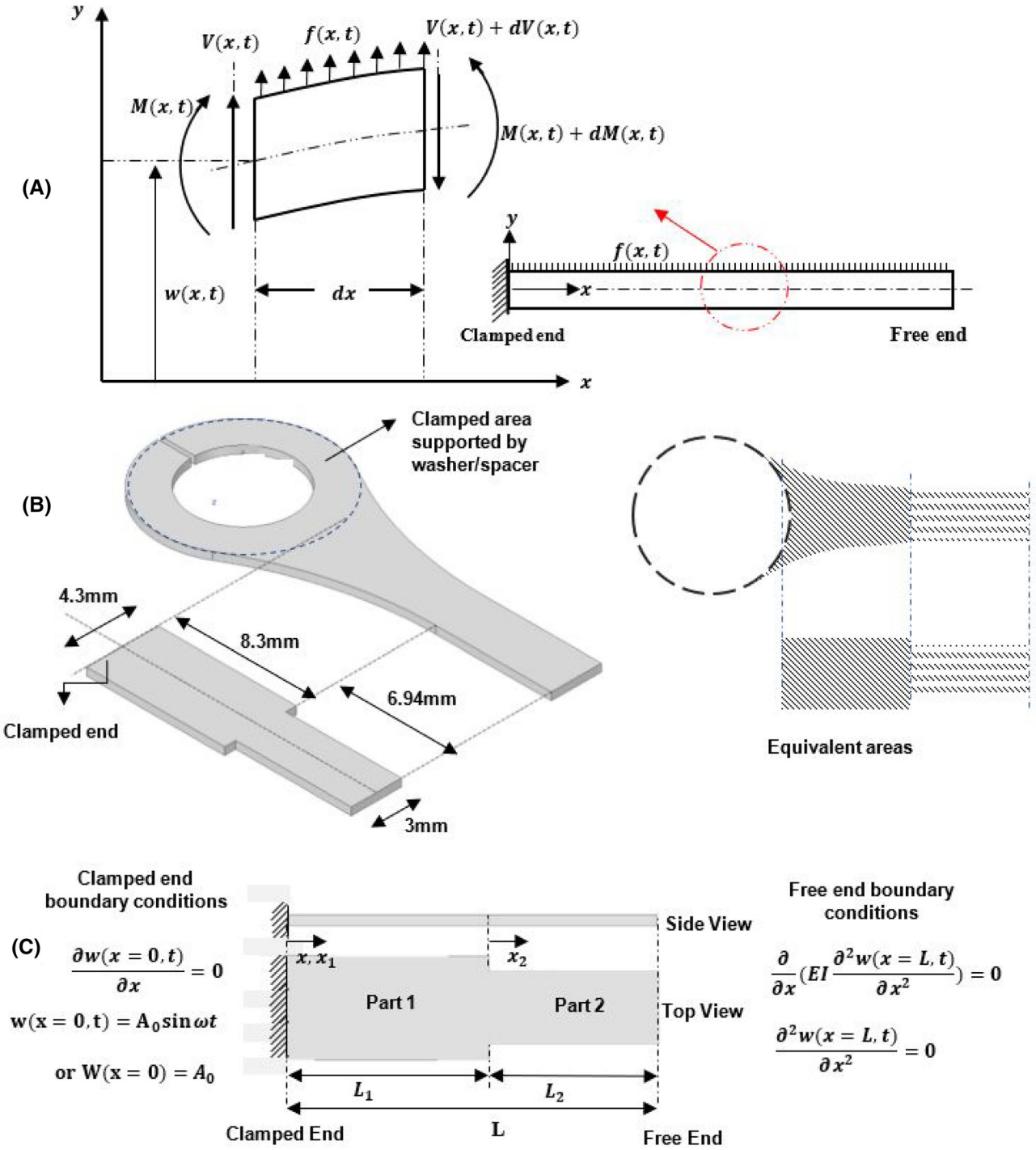

FIGURE 8 (A) Schematic presentation of a cantilever beam, supports, applied loads, and internal force. (B) Equivalent beam model. (C) Boundary conditions applied in the theoretical solution [Colour figure can be viewed at wileyonlinelibrary.com]

moment and shear force, respectively. The change in the internal moment and shear force is denoted by dM and dV.

Using the Newton's second law, the inertia force is calculated for a horizontal beam element with the length of dx (beam axis is in x direction), cross-section area of $A(x)$, and deflection in y direction, $w(x,t)$. By including the inertial force, the equilibrium of the forces in y direction and the moment equilibrium about z axis is considered as below:

$$-(V+dV)+f(x,t)dx+V=\rho A(x)\,dx\frac{\partial^2 w(x,t)}{\partial t^2}, \quad (1)$$

$$(M+dM)-(V+dV)dx+f(x,t)\,dx\frac{dx}{2}-M=0, \quad (2)$$

where ρ is the density of the beam material, t is time, and the term $\frac{\partial^2 w(x,t)}{\partial t^2}$ represents the acceleration of the body in y direction. By replacing $dV=\frac{\partial V}{\partial x}dx$ and $dM=\frac{\partial M}{\partial x}dx$ (ignoring $dx\times dx$ terms), one can arrive at the Equations 3 and 4.

$$-\frac{\partial V(x,t)}{\partial x}+f(x,t)=\rho A(x)\frac{\partial^2 w(x,t)}{\partial t^2}, \quad (3)$$

$$\frac{\partial M(x,t)}{\partial x}-V(x,t)=0. \quad (4)$$

By incorporating Equation 4 into the beam bending theory, the bending moment can be written as $M(x,t)=EI(x)\frac{\partial^2 w(x,t)}{\partial x^2}$. This equation explains the relationship between the bending moment and beam deflection in which $EI(x)$ represents the flexural rigidity. E is the modulus of elasticity and $I(x)$ is the second moment of inertia of the beam's cross-section area. $I(x)$ is calculated with respect to the z axis crossing in the centroid of the cross-section area of $A(x)$. The cross-section area is considered to vary in the x direction; thus, $A(x)$ and $I(x)$ are functions of location. Accordingly, for a beam with uniform section profile in length $I(x)=I$ and $A(x)=A$. Equation 3 is substituted for M and V to obtain the following equation for the forced transverse vibration of a beam (or dynamic beam equation).

$$\frac{\partial^2}{\partial x^2}\left(EI(x)\frac{\partial^2 w(x,t)}{\partial x^2}\right)+\rho A(x)\frac{\partial^2 w(x,t)}{\partial t^2}=f(x,t). \quad (5)$$

The above is the equation for dynamic Euler–Bernoulli beam or the Euler–Lagrange equation for a beam with variable cross-section in length (x direction) and the applied external distributed force of $f(x,t)$ in length of the beam.[51,52] The term $c(x)\frac{\partial w(x,t)}{\partial t}$ may be added to the left side of the Equation 5 in order to consider the damping coefficient of $c(x)$ over the length of the beam.[51]

For a homogeneous beam with uniform cross-section area along the length—where E, I, and A are not dependent on x—the dynamic Euler–Bernoulli turns to the following equation.

$$EI\frac{\partial^4 w(x,t)}{\partial x^4}+\rho A\frac{\partial^2 w(x,t)}{\partial t^2}=f(x,t). \quad (6)$$

Equation 6 is a fourth-order partial differential equation (PDE) which describe the relationship between the applied vertical time-varying distributed load (represented by $f(x,t)$) and the beam's transverse displacement (represented by $w(x,t)$). In absence of the external forces, $f(x,t)$ is equal to zero.

3.1.1 | Analytical: Equivalent beam model

As mentioned earlier, the baseline design fails near the root due to stress concentrations (Figure 4). The optimized design (Figure 5) has a smooth, rounded edge bevel near the root regions, in comparison with the baseline design. In order to solve Equation 6 analytically, the chamfered design is represented by a simple continuous cantilever beam with a step in the middle (cantilever beam with two prismatic parts). Equivalent area approach is used for the geometry simplification (Figure 8B).

In this study, the clamped end of the cantilever beam in Figure 8 is subjected to a vertical reciprocating displacement with an amplitude equal to A_0. Because the amplitude of the lower end of the horn is sinusoidal, the boundary condition for the clamped end is described by a displacement equal to $w(x=0,t)=A_0\sin\omega t$. In this equation, t represents time, and ω is the angular frequency ($\omega=\frac{2\pi}{T}=2\pi f$, where f represents the test frequency of 20 kHz and T refers to the period). Also, because the slope is zero at the clamped end, then $\frac{\partial w}{\partial x}=0$. In addition, the bending moment and shear force are both zero at the free end of the modeled beam so $\frac{\partial^2 W}{\partial x^2}=0$ and $\frac{\partial}{\partial x}\left(EI(x)\frac{\partial^2 W}{\partial x^2}\right)=0$ (the applied boundary conditions are shown in Figure 8C).

Each part of the beam at Figure 8C has a uniform cross-section throughout its length; thus, $I(x)=I$ and $A(x)=A$. Because there are no external forces during the fatigue test, $f(x,t)$ is equal to zero. As a result, Equation 6 takes the form shown below, where $c=\sqrt{\frac{EI}{\rho A}}$.

$$c^2\frac{\partial^4 w(x,t)}{\partial x^4}+\frac{\sigma^2 w(x,t)}{\sigma t^2}=0. \quad (7)$$

For solving the above equation, one can assume $w(x,t)=W(x)T(t)$ based on the separation of variables. When the proposed form of the solution in Equation 7 is replaced and rearranged, the equation below is formed.

$$\frac{c^2}{W(x)}\frac{d^4W(x)}{dx^4}=-\frac{1}{T(t)}\frac{d^2T(t)}{dt^2}=\omega^2, \quad (8)$$

where ω^2 is a positive constant and ω represent the angular velocity. Separate form of the Equation 8 adds two following equations, where $\beta^4=\frac{\omega^2}{c^2}=\frac{\rho A\omega^2}{EI}$.

$$\frac{d^4W(x)}{dx^4}-\beta^4W(x)=0, \quad (9)$$

$$\frac{d^2T(t)}{dt^2}+\omega^2T(t)=0. \quad (10)$$

The solution for Equation 9 is proposed as $W(x)=Ce^{sx}$, where C is a constant. By substituting this solution in Equation 9, one arrives at $s^4-\beta^4=0$. Because the roots of s for the latter equation are $s_{1,2}=\pm\beta$ and $s_{3,4}=\pm i\beta$, the final solution form for Equation 9 can be written as in Equation 11, where C_1 to C_4 are constants obtained from the boundary condition. Moreover, the final form of the solution to Equation 10 is Equation 12.

$$W(x)=C_1\cos\beta x+C_2\sin\beta x+C_3\cosh\beta x+C_4\sinh\beta x, \quad (11)$$

$$T(t)=A\cos\omega t+B\sin\omega t. \quad (12)$$

For the equivalent beam model, in order to take into account the impact of the sudden shift in cross-section, two separate coordinate systems x_1 and x_2, as shown in Figure 8C, are considered. Here, x_1 is $0\le x\le L_1$, and x_2 is as $L_2\le x\le L, x_2(at\,x=L_1)=0, x_2(at\,x=L)=L_2$. Also, as $\beta^4=\frac{\omega^2}{c^2}=\frac{\rho A\omega^2}{EI}$, for each part of the cantilever beam a separate β is described as below:

Consequently, after solving Equation 11, separate equations for each of the two beam sections are derived as follows:

$$W_1(x_1)=C_{11}\cos\beta_1x_1+C_{21}\sin\beta_1x_1+C_{31}\cosh\beta_1x_1+C_{41}\sinh\beta_1x_1, \quad (13)$$

$$W_2(x_2)=C_{12}\cos\beta_2x_2+C_{22}\sin\beta_2x_2+C_{32}\cosh\beta_2x_2+C_{42}\sinh\beta_2x_2, \quad (14)$$

In Equations 13 and 14, constants $C_{11}, C_{21}, C_{31}, C_{41}, C_{12}, C_{22}, C_{32}$, and C_{42} are calculated by solving the equations considering four boundary conditions at the fix and free ends and four continuity conditions of cross-section change point at $x=x_1=L_1$ or $x_2=0$. At the point of discontinuity, vertical displacements/deflections, slope of the beam, internal bending moments, and internal shear forces of the beam in Parts 1 and 2 are equal. $W_1(x_1)$ and $W_2(x_2)$ functions are generated by solving boundary and continuity equations and calculating the constants. The following are the continuity conditions:

$$W_1(x_1=L_1)=W_2(x_2=0), \quad (15)$$

$$\frac{\partial W_1(x_1=L_1)}{\partial x_1}=\frac{\partial W_2(x_2=0)}{\partial x_2}, \quad (16)$$

$$EI_1\frac{\partial^2W_1(x_1=L_1)}{\partial x_1^2}=EI_2\frac{\partial^2W_2(x_2=0)}{\partial x_2^2}, \quad (17)$$

$$\frac{\partial}{\partial x}\left(EI_1\frac{\partial^2W_1(x_1=L_1)}{\partial x_1^2}\right)=\frac{\partial}{\partial x}\left(EI_2\frac{\partial^2W_2(x_2=0)}{\partial x_2^2}\right). \quad (18)$$

Accordingly, the equivalent matrix form of the eight equations mentioned above is given below:

$$\begin{bmatrix} 1 & \cdots & 0 \\ \vdots & \ddots & \vdots \\ B_1\beta_1^3\sin\beta_1L_1 & \cdots & -B_2\beta_2^3 \end{bmatrix}\times\begin{bmatrix} C_{11} \\ \vdots \\ C_{42} \end{bmatrix}=\begin{bmatrix} A_0 \\ \vdots \\ 0 \end{bmatrix}. \quad (19)$$

For Part 1 $(0\le x\le L_1)$ $\beta=\beta_1, I=I_1, A=A_1, width=B_1, \text{and}\ {\beta_1}^4=\frac{\omega^2}{c_1^2}=\frac{\rho A_1\omega^2}{EI_1}.$

For Part 1 $(L_1\le x\le L_2)$ $\beta=\beta_2, I=I_2, A=A_2, width=B_2, \text{and}\ {\beta_2}^4=\frac{\omega^2}{c_2^2}=\frac{\rho A_2\omega^2}{EI_2}.$

After solving the above-mentioned equations obtaining $W_1(x_1)$ and $W_2(x_2)$ functions, $T(t)$ also should be solved in order to find the final answer for $w(x,t) = W(x)T(t)$ equation. The oscillations begin at time $t = 0$, when the displacements, and thus, the vertical deflections are zero (Figure 1). So, when solving Equation 12, the A constant is zero. In addition, at time when $\omega t = \frac{\pi}{2}$, the amplitude reaches its maximum value of A_0; therefore, $B = 1$. Consequently, the solution for Equation 12 is $T(t) = \sin\omega t$ and $w(x,t) = W(x)T(t)$ is explained.

3.1.2 | Analytical: Natural frequencies

The natural frequencies of an undamped system (for the equivalent beam model presented in Figure 8B) with no external forces (and with $A_0 = 0$) can be determined by solving the related eigenvalue problem, which yields an equation identical to Equation 19 when the right side of this equation is set to be zero. The trivial solution to the eigenvalue equation is $C_{11}, C_{21}, C_{31}, C_{41}, C_{12}, C_{22}, C_{32}$, and $C_{42} = 0$. The nontrivial solution is obtained by setting the determinant of the coefficient matrix to zero which yields the following equation. For each natural frequency, the following equation produces ω_n values, where n is the natural mode number and ω is the angular velocity.

$$\begin{vmatrix} 1 & \cdots & 0 \\ \vdots & \ddots & \vdots \\ B_1\beta_1^3 \sin\beta_1 L_1 & \cdots & -B_2\beta_2^3 \end{vmatrix} = 0. \quad (20)$$

3.1.3 | Test specimen design criterion No. 1

Analytical solution for vibration response of the test specimen provides a deep knowledge for the specimen design. A computer program is written using MATLAB to solve the analytical equations listed in Section 3.1 for the equivalent beam model (Figure 8B). The material properties (such as density and Young's modulus) can be found in Table 2. To show the vibration response of the equivalent beam and investigate the effect of the excitation frequency on the transverse deflections of the specimen, the vertical displacement amplitudes of the free-end point of the equivalent beam ($x = L = L_1 + L_2$ or $x_2 = L_2$) are calculated by determining $W_2(x_2 = L_2)$ under different excitation frequencies (frequency range from 0 to 35 kHz)—see Figure 9A. The first, second, and the third natural frequencies can be found in Figure 9A. As expected, due to the resonance, the vertical deflection (vibration) amplitude of the target point ($x_2 = L_2$) increases in frequencies close to the resonance natural frequencies of the beam. In addition, Figure 9B–D depicts the bending mode shape for the modeled equivalent beam at resonant natural frequencies (at times when $\omega t = \frac{\pi}{2}$).

As the vertical displacement of points along a beam is proportional to the induced stress, the excessive displacement/stress distribution near the resonant frequency would hamper the bending-fatigue test. Therefore, test specimen design criterion No. 1: the natural frequencies of the bending-fatigue specimen should be different from the excitation frequency or the natural frequency of the elements in between the specimen and the power supply source, i.e. 20 kHz.

3.1.4 | Test specimen design criterion No. 2

As mentioned in Section 3.1, the internal bending moment can be calculated using $M_z(x,t) = EI(x)\frac{\partial^2 w(x,t)}{\partial x^2}$ for any point along the beam. Furthermore, the maximum normal stress in x direction can be obtained using $\sigma_{Max} = \frac{cM_z}{I}$ (where c is the maximum vertical distance—in y direction—away from the neutral axis of the beam and is equal to half of the beam's thickness). Based on the above explanations and the formulation provided in Section 3.1, the internal bending moment distribution and the normal stress distribution throughout the length of the beam (specimen) are obtained.

When a beam vibrates in its first and third bending modes, the maximum internal bending moment and, consequently, the maximum normal stress occur in a location close to the fixed end of the beam. Figure 10D, E shows the internal bending moment distribution along the beam's length while the beam vibrates below the first mode and above the third bending mode. The optimized test specimen is designed for the second bending mode with the 20-kHz excitation force in between the second and the third natural frequencies (Figure 9A). As a result, in $f = 20$ kHz, the vibration (deflections) amplitude of the specimen is not affected by the resonance phenomenon and the deflection amplitudes/corresponding stresses remain within acceptable range for fatigue studies (design criterion No. 1). For the optimized specimen design, design criterion No. 2 is applied and the internal bending moment distribution graph is shown in Figure 10C. The maximum internal bending moment and deflection ($Max.\,|W - A_0|$) occur in the same position on the beam, which are away from the root and correspond to the location of the maximum normal stress. Changing the amplitudes of the excitation vibration (A_0), fixed at

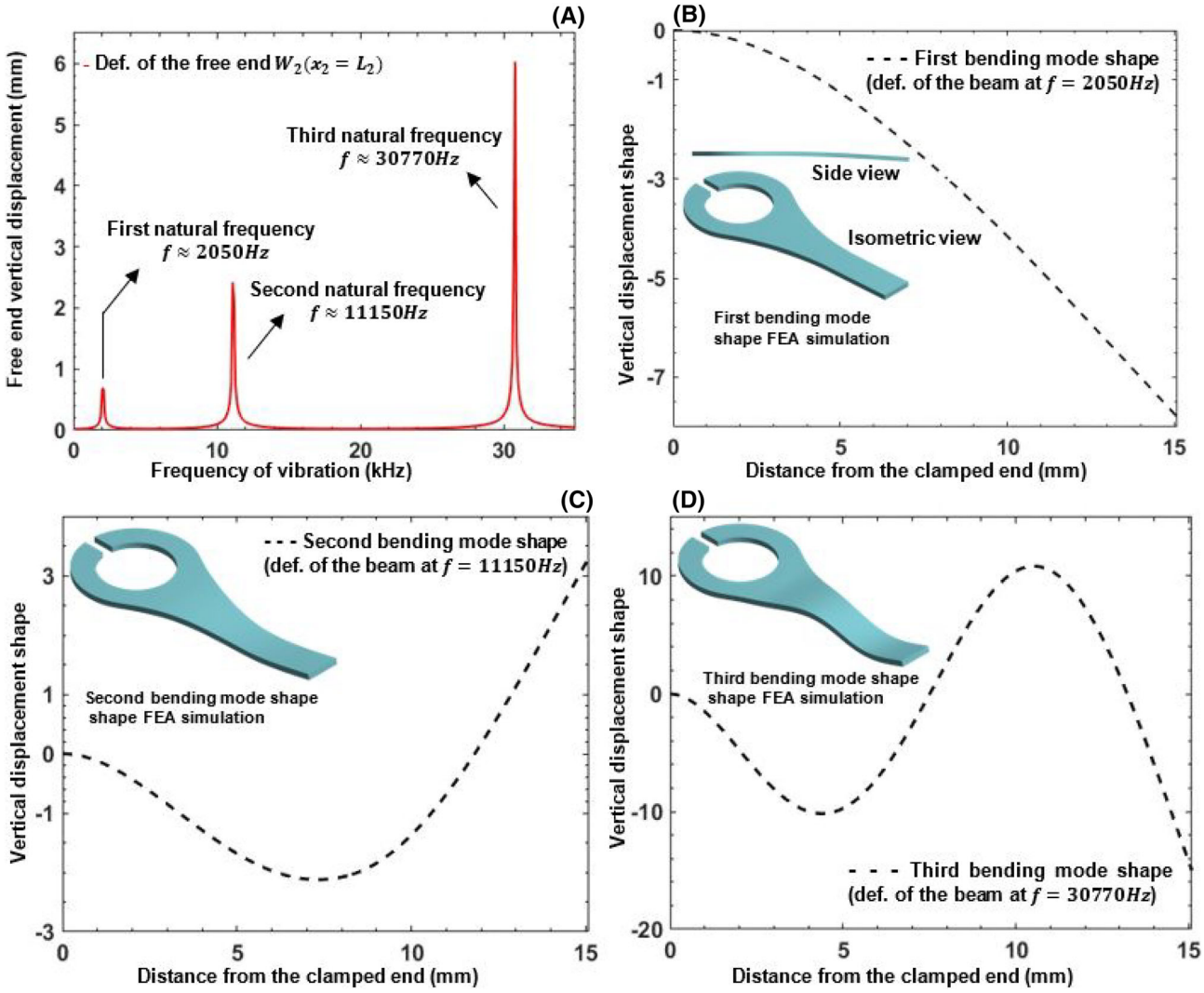

FIGURE 9 (A) The deflection amplitudes of the free-end point of the simplified equivalent beam ($x_2 = L_2$) under different excitation frequencies. (B) First, (C) second, and (D) third bending mode shape via the analytical model (the finite element results are used for the purpose of illustrating the deflection modes) [Colour figure can be viewed at wileyonlinelibrary.com]

20 kHz, produces the same vibration shapes with different vertical displacements (W values) for the specimen. Hence, different maximal stress values can be generated at the gauge section by altering the amplitude of the excitation force. As a result, various stress levels of bending-fatigue tests can be studied via this setup.

For the small-sized bending-fatigue specimen following the two design criteria, Figure 10A illustrates the specimen shape at times when $\omega t = \frac{\pi}{2}$ and $\omega t = \frac{3\pi}{2}$ for a particular case where the horn's tip displacement is 20 μm ($A_0 = 20\,\mu m$). Also, Figure 10B demonstrates the change in the profile of the test specimen between times $t = 0$ and $t = \frac{T}{4}$ (where T is period of cycles) at four divisions. As it can be seen, the position with the maximum displacement (location of $Max.\,|W - A_0|$), with respect to the unchanged shape of the specimen (shape of the test specimen in time $t = 0$) in a specific vertical displacement is always in the gauge section of the specimen where the distance from the clamped end is ≈9.5 mm (also see Figure 5).

3.2 | Finite element analysis

Finite element method is commonly used for analyzing the load and strain distribution in a proposed design under operational conditions.[53–55] In order to find the optimal design, studying the natural frequency of bending-fatigue/straight rod specimens and the stress distribution under different modes of vibration is required. To this end, ANSYS Workbench software package is used for FEA simulations. The final output of

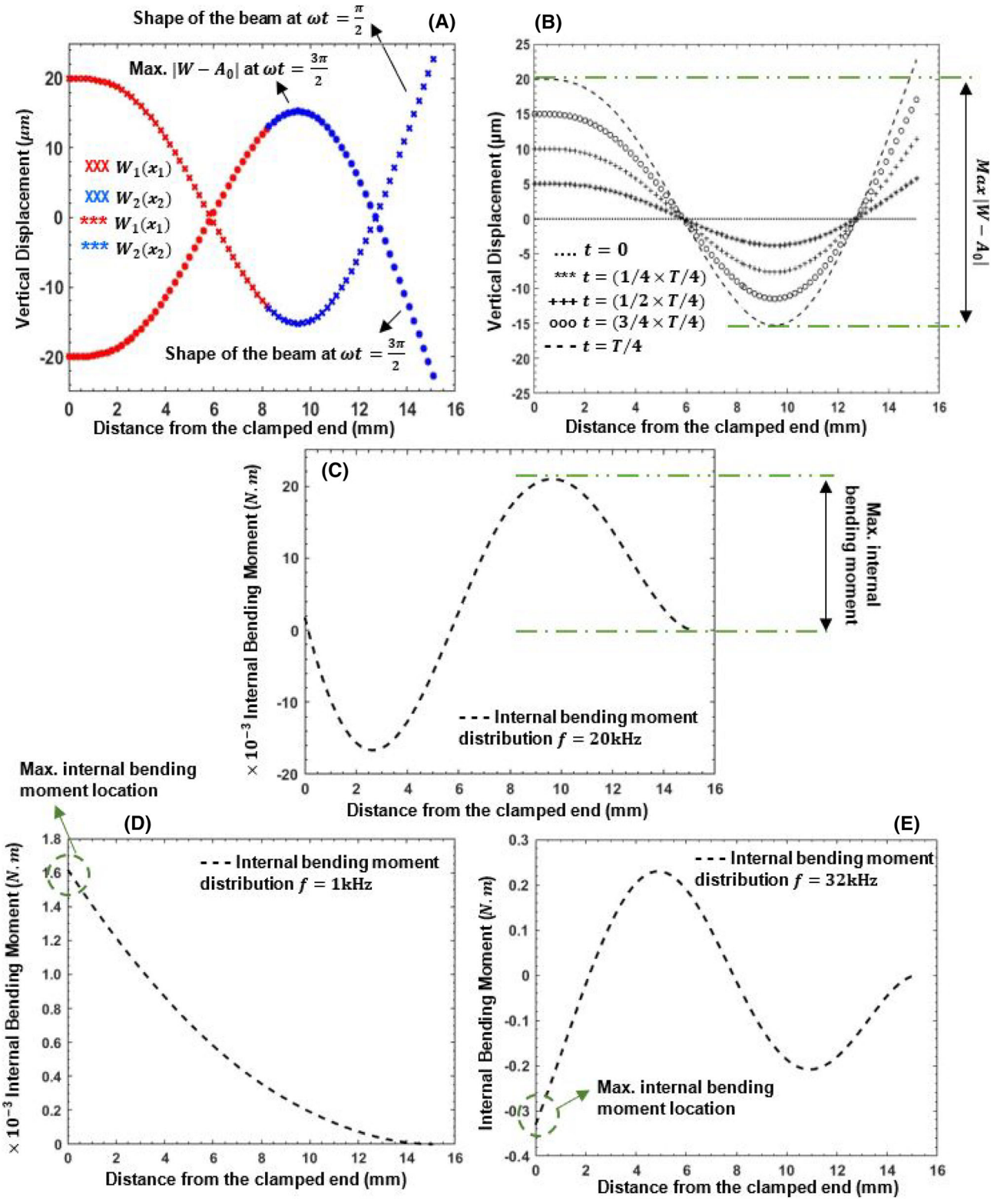

FIGURE 10 Analytical solution showing (A) the shape of the beam at $\omega t = \frac{\pi}{2}$ and $\frac{3\pi}{2}$; (B) the shape of the beam in a cycle from time $t = 0$ to $t = \frac{T}{4}$ for $A_0 = 20\,\mu m$, $f = 20\,kHz$; and (C–E) the internal bending moment distribution under three different excitation frequencies (20, 1, and 32) and $A_0 = 20\,\mu m$ [Colour figure can be viewed at wileyonlinelibrary.com]

the applied acoustic wave by the fatigue tester is in the form of forced vibrating displacement at 20-kHz frequency. Hence, different oscillatory displacement amplitudes (as measured by the eddy-current sensor) ranging from 10 to 50 μm are applied to the ring-like end of the models.

The geometry of the proposed specimens is drawn in the ANSYS Design Modeler environment and meshed with the 8-node quadratic SOLID185 ANSYS elements. A mesh analysis is performed to ensure mesh independence. It is found that a total of 29,000 elements/137,593 nodes are adequate. During the simulations, a modal analysis is first performed to verify the mode shapes at different natural frequencies. Subsequently, a harmonic analysis is performed to obtain the stress/strain distribution at given cyclic displacement amplitudes and 20-kHz frequency.

4 | RESULTS AND DISCUSSION

Prior to conducting the tests, the results of the FEA simulations and the theoretical solution were employed

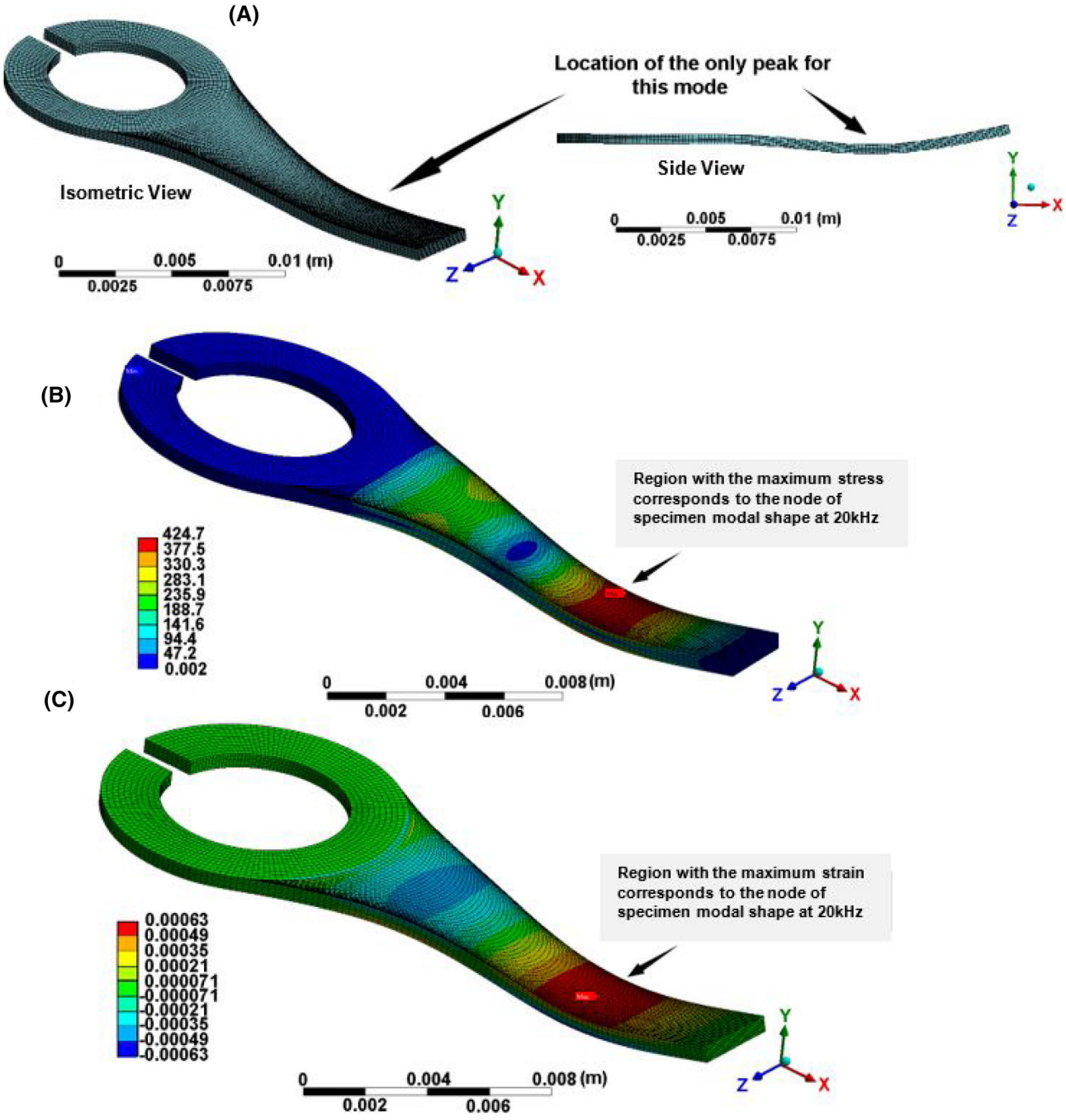

FIGURE 11 (A) The mode shape and the location of the only peak in this vibration mode (at 20 kHz) obtained via finite element modal analysis. (B) Finite element analysis (FEA) simulation result for the equivalent stress distribution across the specimen. The values shown in the legend are in MPa and (C) FEA simulation result for strain distribution (in y direction) through the specimen under 48.9 μm displacement amplitude ($A_0 = 48.9$ μm) and 20-kHz frequency [Colour figure can be viewed at wileyonlinelibrary.com]

to ensure that the proposed design behaves in a desirable manner. The natural frequencies, bending modes, vibration shapes, deflections, and stress distribution along the designed fatigue test specimens were reliably determined and studied using numerical FEA as described in Section 3.2. Additionally, the theoretical solution put forward in Section 3.1 was employed to rapidly explore the designed specimen's vibrational

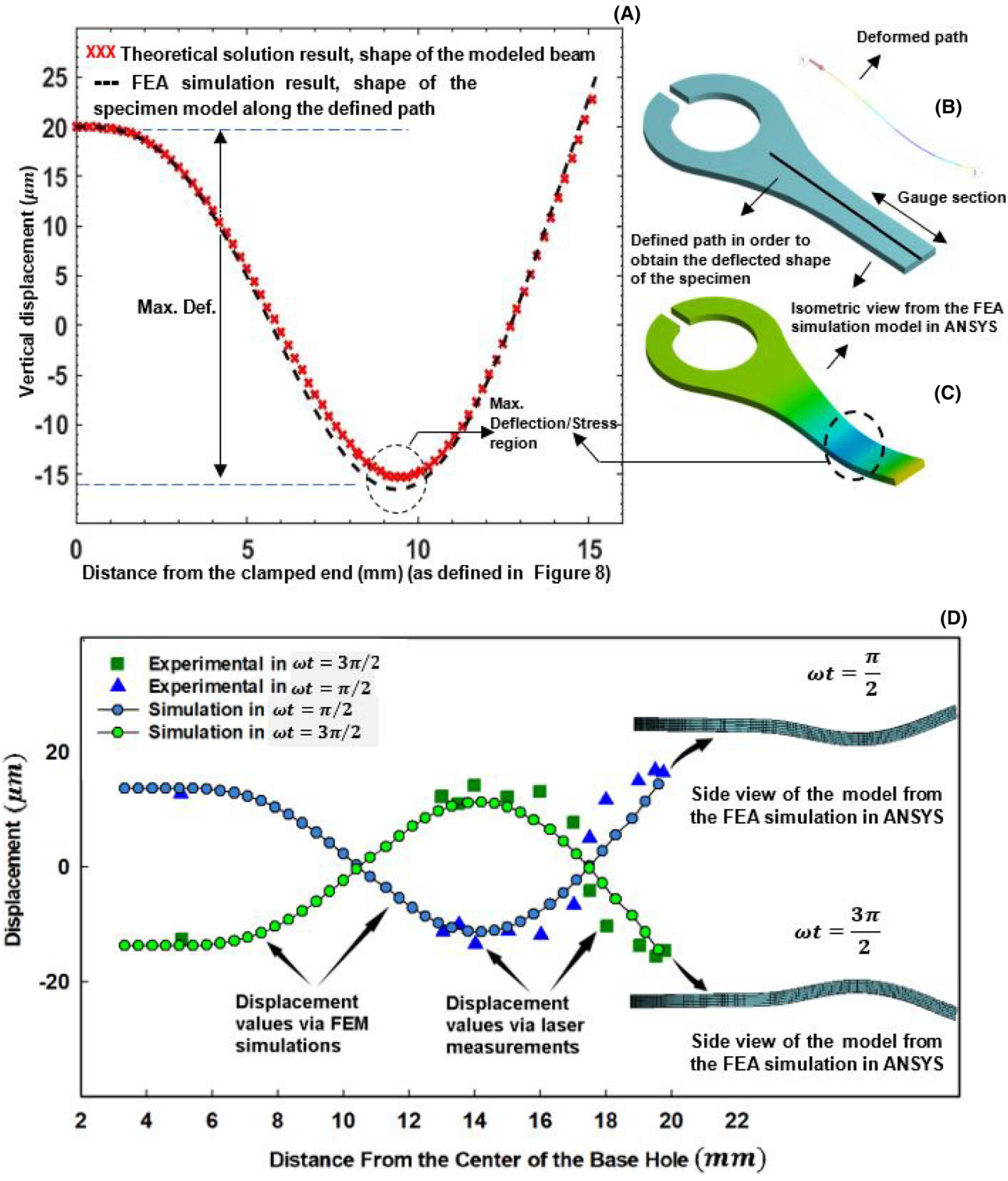

FIGURE 12 (A) Comparing the results for the deflected shape of the beam/specimen form the theoretical solution and the finite element analysis (FEA) simulation for at $\omega t = \frac{\pi}{2}$, $f = 20$ kHz, and $A_0 = 20$ μm; (B) defined path in FEA model; (C) maximum deflection/stress region in FEA simulation; and (D) displacement across the gauge section of the optimized designed specimen via laser displacement measurements and FEA simulation [Colour figure can be viewed at wileyonlinelibrary.com]

response and to obtain a better understanding of the bending modes and the effects of frequency/base amplitude on the vibration shape of the specimen. The theoretical solution with the simplified geometry based on the beam theory also served to compare against the results of the FEA simulations where the complete model form was used. The results with the two methods are consistent.

Multiple configurations were modeled, simulated numerically, built, and tested. The vibration shape and failure behavior of these configurations were studied to achieve an optimal design for the specimen. In Section 2.3, two of the examined designs were introduced. To evaluate and compare the performance of the two designs, the bending-fatigue test was conducted with both of the baseline (Figure 4) and optimized (Figure 5) designs. Because of the high-stress concentration in the base corners, the baseline specimens unanimously broke from this area in all the experiments. Hence, the final proposed design (see Figure 5) is used and proposed for the high-frequency bending-fatigue tests.

Based on results from the FEA simulations (shown in Figure 11) and the theoretical solution (shown in Figure 10), the final proposed design indicates the desired and proper bending mode shape (second mode of bending as shown in Figure 10) at the system testing frequency of 20 kHz. With the gauge section away from the ring (Figure 5), the second bending mode is the proper shape and ideal bending mode for the bending-fatigue test specimen.

To obtain the distribution of stress/strain through the specimen, the displacement amplitudes derived from the

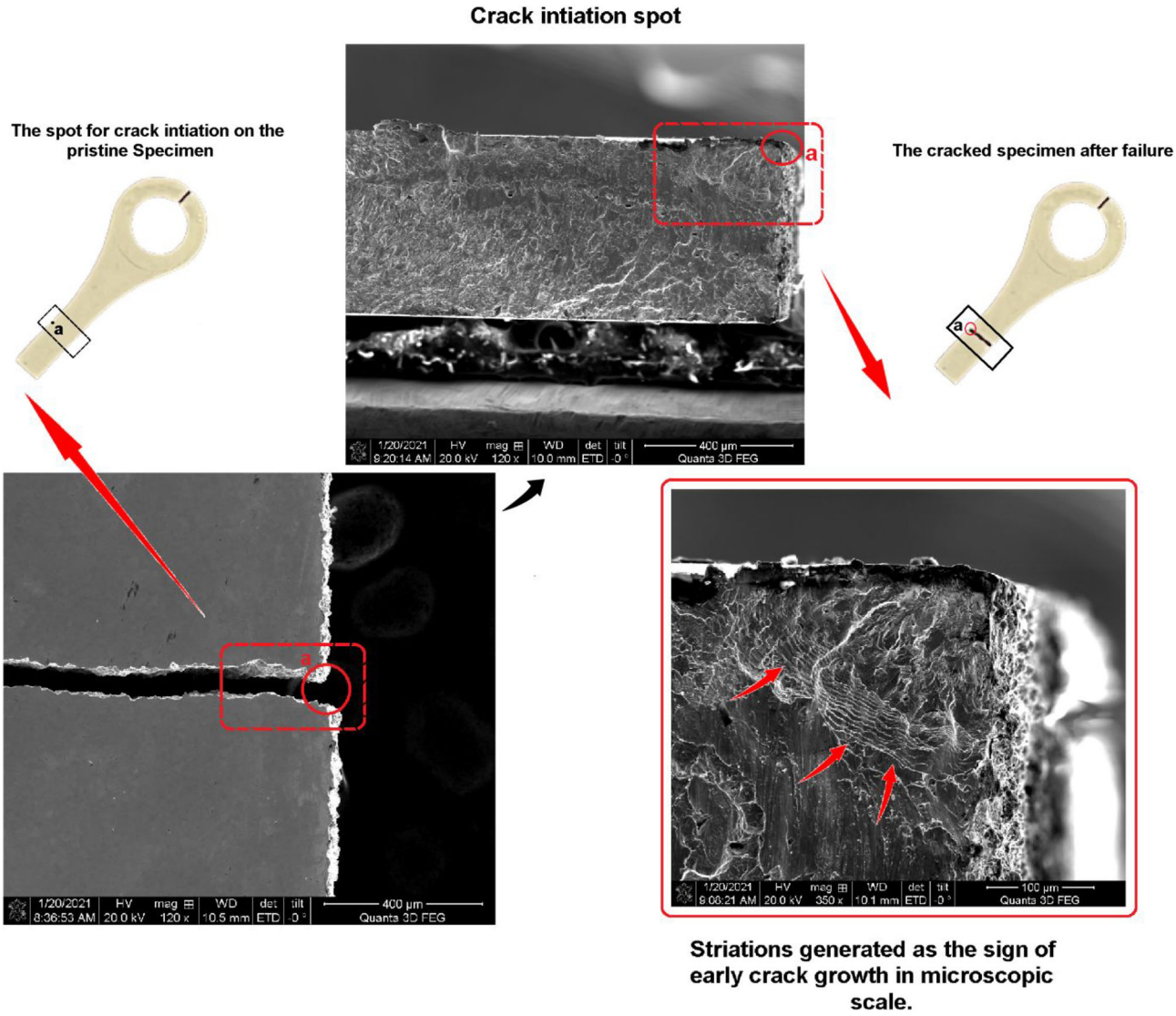

FIGURE 13 Crack initiating in the gauge section for the optimized specimen design [Colour figure can be viewed at wileyonlinelibrary.com]

eddy-current sensor (Figure 3) are used in a harmonic response analysis. FEA simulation results display the equivalent (von Mises) stress distribution along the specimen as presented in Figure 11A. The peak of the mode shape (Figure 11), where maximal bending deflection occurs has the highest stress value. Furthermore, the strain distribution through the specimen (Figure 11C) reveals that the greatest damaging deflection occurs in the same region as the maximum equivalent stress (Figure 11B). The findings of the theoretical approach also agree with the FEA simulation's results for the maximum vertical deflection and, by extension, the maximum stress position.

Moreover, Figure 12A compares the theoretical solution with the results of the ANSYS FEA simulations. The deflections amplitudes along the specimen are measured for the horn's tip displacement amplitude of 20 μm ($A_0 = 20$ μm), the vibration frequency of $f = 20$ kHz, and the time t when $\omega t = \frac{\pi}{2}$ or $\omega t = 2n\pi + \frac{\pi}{2}$ (where $n = 0, 1, \ldots$).

To further verify and ensure the desirable behavior of the proposed design under testing, the displacements along the length of the specimen's gauge section is obtained via the laser displacement sensor (as explained in Figure 7) and compared against the calculations via FEA simulation. In Figure 12D, the experimental readouts and numerically determined values for upward (at times when $\omega t = \frac{3\pi}{2}$) and downward (at times when $\omega t = \frac{\pi}{2}$) bends are plotted. Figure 12D is plotted for the applied horn's tip displacement amplitude of 12.4 μm ($A_0 = 12.4$ μm) and the vibration frequency of $f = 20$ kHz. The experimental and simulation results are in good agreement.

To further evaluate and gain more insight on the optimized test specimen's behavior until failure, the fatigued samples were studied under SEM. In all of the tests, the test specimens consistently broke from the desired gauge section region. This observation is consistent with the results of studying the position of the maximum deflection and stress. Furthermore, the fracture locations found from the experiments are consistent with the locations of the maximum stress/deflection obtained via both the theoretical solution and the FEA simulation. The location of the break on the test specimens and the fractured cross-section SEM image are shown in Figure 13.

High-frequency bending-fatigue test (with zero mean stress) was carried out by employing the test setup described in Section 2.2. The tests were stopped and fatigue lives were recorded once the specimens visibly break and fail. Also a run-out point was considered when a specimen did not break or show any sign of a looming failure after around 40 million cycles. The obtained stress–life Wohler curve derived from the tests results is presented in Figure 14. The variations of life cycles with stress follows a Weibull function on a normal-log plot, which is commonly seen in the literature. The stress amplitudes in Figure 14 are the stress values obtained via FEM that correspond to the applied displacement amplitude of testing.

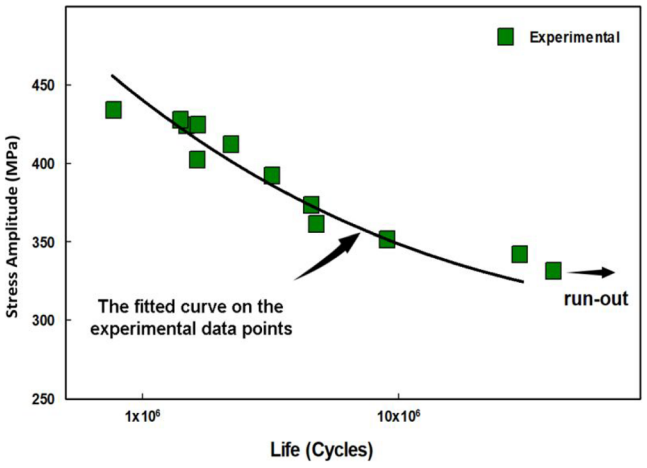

FIGURE 14 Fatigue life at different stress amplitudes (with zero mean stress) for high-frequency bending-fatigue test employing the proposed small-sized specimen design for Inconel alloy 718 material using SHIMADZU fatigue testing system [Colour figure can be viewed at wileyonlinelibrary.com]

It is well known that in the VHCF regimes, the microstructural defects that exist through the material thickness appear to be strong stress raisers. In Figure 14, when approaching the VHCF, the rate of decline with decreasing the load/stress amplitude significantly decreases and gradually stabilizes. This merely indicates that the fatigue limit is being approached, where the stress level is not highly sufficient to trigger the initiation and growth of microcracks from these points. Such behavior further indicates the reliability of the obtained curve.

5 | SUMMARY AND CONCLUSIONS

A design methodology for a small-sized test specimen is put forward with the provision for bending-fatigue experiments via high-frequency fatigue tester systems, and the findings were compared with experimental results. The proposed design is modeled using the finite element method, and modal analysis is performed to investigate the natural frequencies and mode shape of the specimen at frequency of $f = 20$ kHz. The displacement and stress/strain distribution through the test specimen are both determined using harmonic analysis. Theoretical solution is used to rapidly screen the specimen design and provide the understanding to the vibration behavior.

Commercial Inconel alloy 718 sheet metal is used to verify the performance of the proposed design. The laser displacement sensor measurements showed good consistency with the theoretical solutions and FEA simulation results. SEM observations on Inconel 718 bending-fatigue specimens reveal that the crack begins in the gauge section of the specimen and the specimen breaks from the expected location, confirming the FEA simulation and the theoretical solution results. Finally, stress–life Wohler curve is obtained and plotted.

The proposed thin-plate small-sized design ensures that the test specimen performs properly during bending-fatigue experiments, avoiding premature failure due to stress concentration. With the emergence of high-frequency testers and the needs for HCF/VHCF testing outcomes for novel and hard-to-get materials, the proposed thin-plate small-sized design offers an cost-effective approach for rapid testing of fatigue life.

ACKNOWLEDGMENTS

This work is supported by the US National Science Foundation under Grant OIA-1946231 and the Louisiana Board of Regents for the Louisiana Materials Design Alliance (LAMDA). HG, MN, and SG are also partially supported by U.S. Department of Energy under Award Number DE-SC0019378. The authors acknowledge and thank Dr. Congyuan Zeng for SEM imaging and Dr. Hao Wen for laser displacement sensor assembly and setup.

CONFLICT OF INTEREST

The authors declare no conflict of interest.

AUTHOR CONTRIBUTION

Hamed Ghadimi conducted the formal analysis and investigation, curated the data, visualized the study, prepared the original draft, and reviewed and edited the manuscript. Arash P. Jirandehi designed the methodology, curated the data, validated the results, conducted the investigation, prepared the original draft, and reviewed and edited the manuscript; Mohammadsaber Nemati validated the results and conducted the investigation. Shengmin Guo conceptualized the study, prepared the original draft, reviewed and edited the manuscript, supervised the study, and acquired the funding.

DATA AVAILABILITY STATEMENT

Data will be provided upon request.

NOMENCLATURE

$A(x)$, A	cross-section area (m^2)
A_0	horn tip's displacement amplitude (m)
E	modulus of elasticity (Pa)
f	frequency (Hz)
$f(x)$	applied external distributed force (N)
$I(x)$, I	Second moment of inertia of the cross-section area (m^4)
L	total length of the beam (m)
L_1	length of the Part 1 (m)
L_2	length of the Part 2 (m)
$M(x,t)$, M	internal bending moment (N.m)
T	period (s)
t	time (s)
$V(x,t)$, V	internal shear force (N)
$w(x,t)$	deflection of beam in y direction (m)
x	global x coordinate (m)
x_1	x coordinate for beam Part 1 (m)
x_2	x coordinate for beam Part 2 (m)
y	global y coordinate (m)
z	global z coordinate (m)
ρ	density (kg/m^3)
σ	normal stress (MPa)
ω	angular frequency (rad/s)

ORCID

Hamed Ghadimi https://orcid.org/0000-0002-1887-1002
Arash P. Jirandehi https://orcid.org/0000-0002-9536-2447
Saber Nemati https://orcid.org/0000-0002-7255-2539
Shengmin Guo https://orcid.org/0000-0002-3673-0836

REFERENCES

1. Marines I, Bin X, Bathias C. An understanding of very high cycle fatigue of metals. *Int J Fatigue*. 2003;25(9–11):1101-1107.
2. Stanzl-Tschegg S. Very high cycle fatigue measuring techniques. *Int J Fatigue*. 2014;60:2-17.
3. P. Jirandehi A, M. Khonsari M. General quantification of fatigue damage with provision for microstructure: a review. *Fatigue Fract Eng Mater Struct*. 2021;44(8):1973-1999.
4. Rama Krishna L, Madhavi Y, Sahithi T, et al. Enhancing the high cycle fatigue life of high strength aluminum alloys for aerospace applications. *Fatigue Fract Eng Mater Struct*. 2019;42(3):698-709.
5. Ilie P, Lesperance X, Ince A. Development of an ultrasonic fatigue testing system for gigacycle fatigue. *Mater Des Process Commun*. 2020;2(6):e120.
6. Bathias C. Piezoelectric fatigue testing machines and devices. *Int J Fatigue*. 2006;28(11):1438-1445.
7. Mayer H. Recent developments in ultrasonic fatigue. *Fatigue Fract Eng Mater Struct*. 2016;39(1):3-29.
8. Mayer H. Ultrasonic torsion and tension–compression fatigue testing: measuring principles and investigations on 2024-T351 aluminium alloy. *Int J Fatigue*. 2006;28(11):1446-1455.
9. Xue H, Tao H, Montembault F, Wang Q, Bathias C. Development of a three-point bending fatigue testing methodology at 20 kHz frequency. *Int J Fatigue*. 2007;29(9–11):2085-2093.
10. Huang J, Spowart J, Jones J. Fatigue behaviour of SiCp-reinforced aluminium composites in the very high cycle regime

using ultrasonic fatigue. *Fatigue Fract Eng Mater Struct*. 2006; 29(7):507-517.
11. Lesperance X, Ilie P, Ince A. Very high cycle fatigue characterization of additively manufactured AlSi10Mg and AlSi7Mg aluminium alloys based on ultrasonic fatigue testing. *Fatigue Fract Eng Mater Struct*. 2021;44(3):876-884.
12. Rhein RK, Shi Q, Arjun Tekalur S, Wayne Jones J, Carroll JW. Effect of direct metal laser sintering build parameters on defects and ultrasonic fatigue performance of additively manufactured AlSi10Mg. *Fatigue Fract Eng Mater Struct*. 2021; 44(2):295-305.
13. Costa PR, Montalvão D, Freitas M, Baxter R, Reis L. Cruciform specimens' experimental analysis in ultrasonic fatigue testing. *Fatigue Fract Eng Mater Struct*. 2019;42(11):2496-2508.
14. Wagner D, Cavalieri FJ, Bathias C, Ranc N. Ultrasonic fatigue tests at high temperature on an austenitic steel. *Propul Power Res*. 2012;1(1):29-35.
15. Wu T, Jago G, Bechet J, Bathias C, Guichard D. Accelerated vibratory fatigue test by ultrasonic frequency at cryogenic temperature. *Eng Fract Mech*. 1996;54(6):891-895.
16. Sun Z, Bathias C, Baudry G. Fretting fatigue of 42CrMo4 steel at ultrasonic frequency. *Int J Fatigue*. 2001;23(5):449-453.
17. Ferdous W, Manalo A, Peauril J, et al. Testing and modelling the fatigue behaviour of GFRP composites—effect of stress level, stress concentration and frequency. *Eng Sci Technol Int J*. 2020;23(5):1223-1232.
18. Hajshirmohammadi B, Khonsari M. A simple approach for predicting fatigue crack propagation rate based on thermography. *Theor Appl Fract Mech*. 2020;107:102534.
19. Koymatcik H, Ahlatci H, Sun Y, Turen Y. Effect of carbon content and drawing strain on the fatigue behavior of tire cord filaments. *Eng Sci Technol Int J*. 2018;21(3):289-296.
20. Kashyzadeh KR. A new algorithm for fatigue life assessment of automotive safety components based on the probabilistic approach: the case of the steering knuckle. *Eng Sci Technol Int J*. 2020;23(2):392-404.
21. Najafizadeh N, Rajabi M, Hashemi R, Amini S. Improved microstructure and mechanical properties of sheet metals in ultrasonic vibration enhanced biaxial stretch forming. *J Theor Appl Vib Acoust*. 2019;5(1):1-10.
22. Hajshirmohammadi B, Khonsari M. Thermographic evaluation of metal crack propagation during cyclic loading. *Theor Appl Fract Mech*. 2020;105:102385.
23. Rahmatabadi D, Tayyebi M, Najafizadeh N, Hashemi R. Experimental investigation of formability of Al/Mg/Al strips fabricated via cold roll bonding process. Paper presented at: Proceedings of Iran International Aluminium Conference (IIAC2018); 2018.
24. Habibian S. Analysis and control of Fiber-Reinforced Elastomeric Enclosures (FREEs). arXiv preprint arXiv:191207380. 2019.
25. Ghayoor M, Mirzababaei S, Lee K, He Y, Chang C-H, Paul BK, Pasebani S. Strengthening of 304L stainless steel by addition of yttrium oxide and grain refinement during selective laser melting. Paper presented at: Annual International Solid Freeform Fabrication Symposium: Austin, TX, USA; 2019.
26. Zeng C, Zhang B, Ettefagh AH, et al. Mechanical, thermal, and corrosion properties of Cu-10Sn alloy prepared by laser-powder-bed-fusion additive manufacturing. *Addit Manuf*. 2020;35:101411.
27. Ettefagh AH, Zeng C, Guo S, Raush J. Corrosion behavior of additively manufactured Ti-6Al-4V parts and the effect of post annealing. *Addit Manuf*. 2019;28:252-258.
28. Fitzka M, Pennings B, Karr U, et al. Influence of cycling frequency and testing volume on the VHCF properties of 18Ni maraging steel. *Eng Fract Mech*. 2019;216:106525.
29. Hung C-H, Chen W-T, Sehhat MH, Leu MC. The effect of laser welding modes on mechanical properties and microstructure of 304L stainless steel parts fabricated by laser-foil-printing additive manufacturing. *Int J Adv Manuf Syst*. 2021;112(3): 867-877.
30. Antolovich SD, Jayaraman N. The effect of microstructure on the fatigue behavior of Ni base superalloys. Paper presented at: Fatigue; 1983.
31. Ai Y, Zhu S, Liao D, et al. Probabilistic modeling of fatigue life distribution and size effect of components with random defects. *Int J Fatigue*. 2019;126:165-173.
32. Seifi M, Salem A, Satko D, Shaffer J, Lewandowski JJ. Defect distribution and microstructure heterogeneity effects on fracture resistance and fatigue behavior of EBM Ti–6Al–4V. *Int J Fatigue*. 2017;94:263-287.
33. Makkonen L, Rabb R, Tikanmäki M. Size effect in fatigue based on the extreme value distribution of defects. *Mater Sci Eng A*. 2014;594:68-71.
34. Afkhami S, Dabiri M, Piili H, Björk T. Effects of manufacturing parameters and mechanical post-processing on stainless steel 316L processed by laser powder bed fusion. *Mater Sci Eng A*. 2020;802:140660.
35. Lomakin I, Arutyunyan A, Valiev R, Gadzhiev F, Murashkin MY. Design and evaluation of an experimental technique for mechanical and fatigue testing of sub-sized samples. *Exp Tech*. 2018;42(3):261-270.
36. Li Y, Song Q, Feng S, Sun C. Effects of loading frequency and specimen geometry on high cycle and very high cycle fatigue life of a high strength titanium alloy. *Materials*. 2018;11(9): 1628.
37. Rund M, Volák J, Šindelářová M. Small size specimens methods for evaluation of mechanical properties. *Adv Mat Res*. 2015;1127:1-8.
38. Džugan J, Konopik P, Rund M, Prochazka R. Determination of local tensile and fatigue properties with the use of sub-sized specimens. Paper presented at: Pressure Vessels and Piping Conference; 2015.
39. Ishii H, Taguchi Y, Ishii K, Akagi H. OS11W0239 Ultrasonic bending fatigue testing method for thin sheet materials. Paper presented at: The Abstracts of ATEM: International Conference on Advanced Technology in Experimental Mechanics: Asian Conference on Experimental Mechanics; 2003.
40. Farhad F, Smyth-Boyle D, Zhang X, Wallis I, Panggabean D. Laboratory apparatus for in-situ corrosion fatigue testing and characterisation of fatigue cracks using X-ray micro-computed tomography. *Fatigue Fract Eng Mater Struct*. 2018;41(12): 2629-2637.
41. Wisner B, Mazur K, Kontsos A. The use of nondestructive evaluation methods in fatigue: a review. *Fatigue Fract Eng Mater Struct*. 2020;43(5):859-878.

42. Castelluccio GM, McDowell DL. Microstructure-sensitive small fatigue crack growth assessment: effect of strain ratio, multiaxial strain state, and geometric discontinuities. *Int J Fatigue*. 2016;82:521-529.
43. Wang Q, Apelian D, Lados D. Fatigue behavior of A356-T6 aluminum cast alloys. Part I. Effect of casting defects. *J Light Met*. 2001;1(1):73-84.
44. Hu Y, Wu S, Withers P, et al. The effect of manufacturing defects on the fatigue life of selective laser melted Ti-6Al-4V structures. *Mater Des*. 2020;192:108708.
45. Yoshinaka F, Nakamura T, Takeuchi A, Uesugi M, Uesugi K. Initiation and growth behaviour of small internal fatigue cracks in Ti-6Al-4V via synchrotron radiation microcomputed tomography. *Fatigue Fract Eng Mater Struct*. 2019;42(9):2093-2105.
46. Pedersen MM. Introduction to metal fatigue. *Tech Rep Mech Eng*. 2018;5(11):91-91.
47. Günther J, Krewerth D, Lippmann T, et al. Fatigue life of additively manufactured Ti–6Al–4V in the very high cycle fatigue regime. *Int J Fatigue*. 2017;94:236-245.
48. Siddique S, Imran M, Walther F. Very high cycle fatigue and fatigue crack propagation behavior of selective laser melted AlSi12 alloy. *Int J Fatigue*. 2017;94:246-254.
49. Yang K, He C, Huang Q, et al. Very high cycle fatigue behaviors of a turbine engine blade alloy at various stress ratios. *Int J Fatigue*. 2017;99:35-43.
50. Shimadzu. Observation of bending fatigue testing of metal plate at ultrasonic frequency; 2015. www.shimadzu.com
51. Bashash S, Salehi-Khojin A, Jalili N. Forced vibration analysis of flexible Euler-Bernoulli beams with geometrical discontinuities. Paper presented at: 2008 American Control Conference; 2008.
52. Repetto C, Roatta A, Welti R. Forced vibrations of a cantilever beam. *Eur J Phys*. 2012;33(5):1187-1195.
53. Buffinton KW, Wheatley BB, Habibian S, Shin J, Cenci BH, Christy AE. Investigating the mechanics of human-centered soft robotic actuators with finite element analysis. Paper presented at: 2020 3rd IEEE International Conference on Soft Robotics (RoboSoft); 2020.
54. Habibian S, Dadvar M, Peykari B, et al. Design and implementation of a maxi-sized mobile robot (Karo) for rescue missions. *ROBOMECH J*. 2021;8(1):1-33.
55. Tieying W, Bathias C. Application of fracture mechanics concepts in ultrasonic fatigue. *Eng Fract Mech*. 1994;47(5):683-690.

How to cite this article: Ghadimi H, Jirandehi AP, Nemati S, Guo S. Small-sized specimen design with the provision for high-frequency bending-fatigue testing. *Fatigue Fract Eng Mater Struct*. 2021;1-21. doi:10.1111/ffe.13589